

An alternative mathematical modeling of the scintillation camera and framework for performance analysis of gamma-ray positioning algorithms

Behnoosh Teimourian Fard^{1,2}, Mojtaba Shamsaei Zafarghandi¹,
Soheil Hosseini², Hamid Sabet³, Mohammad Reza Ay^{2,4}

¹Department of Energy Engineering and Physics, Amirkabir University of Technology, Tehran, Iran

²Research Center for Molecular and Cellular Imaging, Tehran University of Medical Sciences, Tehran, Iran

³Massachusetts General Hospital, Harvard Medical School, Boston, Massachusetts, USA

⁴Department of Medical Physics and Biomedical Engineering, Tehran University of Medical Sciences, Tehran, Iran

(Received 8 October 2017, Revised 18 January 2018, Accepted 25 January 2018)

ABSTRACT

Introduction: Substantive amount of work has been done in modeling and analyzing the scintillation camera system processes including positioning and image formation. The goal of this work is to develop a framework for analyzing performance of nonlinear positioning methods upon construction of a mathematical model of the system. In this study, the photodetector array counts are assumed to follow a multinomial distribution.

Methods: We studied effects of several parameters on system performance, including photomultiplier tube (PMT) non-uniform response, gains, shape, size and positioning methods. This was done by constructing linearity and resolution maps, feeding the system a uniform grid of point sources showing the distorted output along with associated blurring intensity. The spatial resolution and linearity parameters are used to evaluate the performance of simulated scintillation camera.

Results: The study findings revealed that the square PMT is the best option due to better fitting and quality especially near the edge of the detector and also ability to cover the rectangular crystal area with minimum numbers of PMTs. Also, the resolution resulted from CSE is 5% and 20% better than center of mass and modified center of mass respectively.

Conclusion: We showed that the rectangular gamma camera accompanied by an array of square PMTs can introduce the optimum performance regarding linearity and resolution if the nonlinear method, called CSE, is used as positioning method. Further evaluation is needed to evaluate the performance of the proposed gamma camera in practice.

Key words: Gamma camera; Square PMT; Mathematical modeling; Multinomial distribution; Nonlinearity Map; Correlated signal enhancement

Iran J Nucl Med 2018;26(2):112-120

Published: July, 2018

<http://irjnm.tums.ac.ir>

Corresponding author: Dr Mohammad Reza Ay, Department of Medical Physics and Biomedical Engineering, Tehran University of Medical Sciences, Tehran, Iran. E-mail: mohammadreza_ay@sina.tums.ac.ir

INTRODUCTION

The gamma camera imaging have played an important role in medical imaging since 50th [1, 2]. The principles of the gamma camera operation are well covered in classic publications [3], along with more recent advancements in review papers as well [4]. Rigorous mathematical analyses followed over the years after the introduction of the camera in 1958 by Hall Anger [1], modeling and analyzing (within day's available computational technology) various aspects of the camera.

Theoretical simulation of the Anger gamma camera system was applied to investigate the dependence of intrinsic resolution and uniformity of the energy-defining pulse on the stochastic nature of the photomultiplier pulse formation and design parameters by Svedberg [5, 6]. Svedberg also presented a computer model to evaluate image quality considering various parameters of gamma camera including crystal dimensions, light guide length and optical properties, number, size and position of the photomultiplier tubes, and type of pulse mixing circuit [7].

Baker et al. investigated a theoretical approach to optimize the design of gamma camera such as light guide thickness, the geometric of array of PMTs, PMT gain and so on [8]. There are more recent computational investigations to design, build and evaluate a scintillation camera [9, 10], although they are more concerned with numerical Monte Carlo models and simulations. Methods based on statistical estimation like maximum-likelihood are also widely popular [11]. The approach taken in this work most resembles that of Fessler [12] in mathematical rigor, and in the interest in analytical prediction of the performances.

In this work, we characterize the linearity and resolution performance of scintillation cameras that using generalized nonlinear model for position estimation of the gamma-ray interaction with scintillation detector. Then we study the effect of varying values of several parameters such as PMT shape and its size, response function and gain variation, crystal thickness on system performance.

METHODS

We describe our model starting with a simple hypothetical scenario and increase the complexity arriving to a realistic model used in our experiments that include arbitrary gamma source collimator geometry, crystal and light-guide thickness, and gamma-ray event positioning arithmetic.

The most basic detection possible scenario would be with a fixed-point source of scintillation photons and a plain un-arrayed photodetector of infinite extent, the source radiating isotropically an infinite number of

photons and the photodetector retaining all photon incidence information.

The number of scintillation photons being infinite $N^* = \infty$, we can assume a continuous flux of energy out from the source changing as $(1/4\pi r^2)$, where r in the distance from the source. We consider the center of mass (com{ }) operator to produce our estimate of the source position. Given the intensity distribution on the detector, this operator performs perfect for noiseless data and yields as positioning output exactly the input coordinates, as com{ } operator of an unbounded symmetrical distribution is found to be the center.

When the infinite photodetector is replaced with one of limited extent the com{ } operator will no longer work perfect. In fact, for any given source coordinates, the estimate produced by the operator will be somewhat attracted towards the center of the detector. We will refer to this effect as the *minimalisation* effect.

In the next step, we consider the case where there is a photodetector array, each array element (or photomultiplier tube, PMT) providing only a single value representing the energy deposited over its surface. The com{ } operator should be calculated discrete: the double integrals of the intensity distribution on the photodetector elements will serve as the weights:

$$I_{11} = \int_0^D \int_{-D}^0 \left(\frac{1}{4\pi r^2} \right) (\hat{r} \cdot \hat{n}) dy dx \Bigg/ \iint_{\text{Whole Detector}} \left(\frac{1}{4\pi r^2} \right) (\hat{r} \cdot \hat{n}) ds \quad (1)$$

Where \hat{n} the unit vector normal to detector, \hat{r} the unit vector outward from the point source, and the element centers, or any other point for that matter, as the locations in localization calculations and D is the diameter of each of PMT.

For any given source position, the positioning algorithm produces a specific output on photodetector elements; With a uniform grid of points as input source positions, we can scatter-plot the resulting warped grid. Note the slight attraction towards PMT centers, namely the *pincushion* effect.

As an illustration of detector elements, we assume this photodetector array consists of a 4×6 array of square PMTs (Figure 1). Unless stated otherwise, the scintillation photons are originated at a distance h from the photodetector plane.

To investigate of finite scintillation photons, we reduce N^* from infinity to a finite number. We further assume that exactly N photons reach the photodetector – a deterministic fraction of N^* determined solely by the solid angle at which it sees the detector. In reality, N is a random variable about this mean value. Unlike previous cases, over repeated scintillation instances at

the same point, we will have, as positioning output, a cloud rather than a single point. We take the first step towards performance characterization by analytically deriving the statistical features of this cloud.

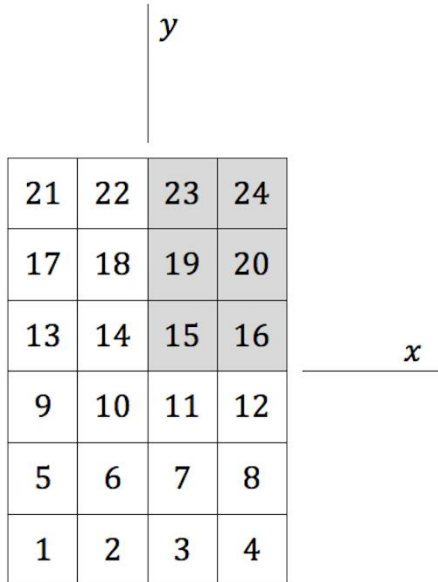


Fig 1. Outline of the photodetector array.

We designate the counts recorded by the PMTs at each scintillation instance as $C_i, i=1...24$. At each instance N photons are distributed among C_i ; the underlying probabilities are also known, namely I_i ; so C , the random column vector containing all C_i , follows a *multinomial distribution* (see *Appendix I* for complete proofs), and we have

$$E(C_i) = NI_i, \text{ Var}(C_i) = NI_i(1 - I_i), \text{ Cov}(C_i, C_j) = -NI_i I_j \quad (2)$$

If we arrange the positions of the PMT centers in a matrix

$$\mathbf{\Pi} = \begin{pmatrix} \rho_{1x} & \dots & \rho_{wx} \\ \rho_{1y} & \dots & \rho_{wy} \end{pmatrix} \quad (3)$$

in which ρ_{ix}, ρ_{iy} are the x, y -coordinates of the i^{th} tube, the output could be expressed as

$$\mathbf{R}_{(2 \times 1)} = \frac{1}{N} \mathbf{\Pi} \mathbf{C} \quad (4)$$

Note that R is a random vector too and we can write:

$$E(\mathbf{R}) = \frac{1}{N} \mathbf{\Pi} E(\mathbf{C}) \quad (5)$$

$$\text{Cov}(\mathbf{R}) = \frac{1}{N^2} \text{Cov}(\mathbf{\Pi} \mathbf{C}) = \frac{1}{N^2} \mathbf{\Pi} \text{Cov}(\mathbf{C}) \mathbf{\Pi}^T \quad (6)$$

Thanks to the extra information we have about C in (1), we know both $E(C)$ and $\text{Cov}(C)$ (See Note in *Appendix I-I*). For example $E(C)$ will be NI in which I is the column vector containing I_i , and $E(\mathbf{R})$ will therefore be identical to that in Part (C), meaning that non-linearity maps are not affected by N^* .

We can use the norm of the two diagonal elements of $\text{Cov}(\mathbf{C})$ as a feature representing the blurring intensity corresponding to each source position, and then construct “resolution” maps, along with non-linearity maps. We can finally use the following relationship to arrive at real FWHM values.

$$\text{FWHM} \cong 2.35\sigma \quad (7)$$

Anger method

As a sample application of the framework developed above, here we consider a generalized positioning scenario, in which the counts C is the first put through non-linear conditioning before proceeding with $\text{com}\{\}$ calculation,

$$\mathbf{R} = \frac{1}{N} \mathbf{\Pi} f(\mathbf{C}). \quad (8)$$

This could be the simple thresholding function that is commonly used in Anger logic to round off small values. The choice of the function largely affects the performance of the method. To characterize the performance, we have

$$E(\mathbf{R}) = \frac{1}{N} \mathbf{\Pi} E(f(\mathbf{C})) \quad (9)$$

$$\text{Cov}(\mathbf{R}) = \frac{1}{N^2} \mathbf{\Pi} \text{Cov}(f(\mathbf{C})) \mathbf{\Pi}^T. \quad (10)$$

To construct $E(f(\mathbf{C}))$ and $\text{Cov}(f(\mathbf{C}))$ we need to construct their constituents, which through definition are

$$E(f(C_i)) = \sum_{k=0}^N f(k) \cdot \text{PDF}_{(C_i)}(k) \quad (11)$$

$$\text{Var}(f(C_i)) = \sum_{k=0}^N f^2(k) \cdot \text{PDF}_{(C_i)}(k) - E^2(f(C_i)) \quad (12)$$

$$\begin{aligned} & \text{Cov}(f(C_i), f(C_j)) \\ &= \sum_{k=0}^N \sum_{l=0}^{N-k} f(k) \cdot f(l) \cdot \text{JOINT}_{(C_i, C_j)}(k, l) \\ & - E(f(C_i)) \cdot E(f(C_j)). \quad (13) \end{aligned}$$

Note that the information that was previously available in (2) is no longer of any help here, and the constituents need to be directly calculated. The marginal distributions $PDF_{(C_i)}$ and $JOINT_{(C_i, C_j)}$ of a multinomial distribution are known from statistics (see *Appendix I-II* for complete proofs).

It should be noted that (11)-(13) represent the general solution, and approximations may further be devised if desired. Also, as can be seen, calculations involve summations over factors that directly involve the number of photons N . The Gaussian approximation to the multinomial distribution can be used at most of the instances, but not all, and therefore the required processing time still increases out of control with increasing N . A smaller $N = 85$ has therefore been used, believing it still can provide us with information about the system behavior.

Note that if f can be approximated by a linear function we would have used the Taylor approximations of $E(f(\mathbf{C}))$ and $Cov(f(\mathbf{C}))$ and bypassed equations (11)-(13). And finally, the function actually used here, normalized to $(0, 1)$, has been $f(x) = \text{ramp}(x - 1/120)$, which is simply a slight variation of the identity function $h(x) = x$; the actual domain is $(0, N)$.

CSE method

Here we consider another nonlinear positioning method in which the column and row sums are first obtained (not direct readings from detector elements), and then passed through nonlinear conditioning and plugged into (one-dimensional) $\text{com}\{\}$ that is called correlated signal enhancement (CSE) [13].

We introduce the vector δ containing column and row sums of the acquired data. We use the simpler 2×3 detector of *Figure 2* for illustration. As can be seen, while \mathbf{C} has (2×3) elements, δ will have $(2 + 3)$.

In matrix form, in terms of \mathbf{C} , δ would naturally be

$$\delta = \begin{pmatrix} 1 & 0 & 1 & 0 & 1 & 0 \\ 0 & 1 & 0 & 1 & 0 & 1 \\ 1 & 1 & 0 & 0 & 0 & 0 \\ 0 & 0 & 1 & 1 & 0 & 0 \\ 0 & 0 & 0 & 0 & 1 & 1 \end{pmatrix} \mathbf{C} = \Theta \mathbf{C} \quad (14)$$

Looking at *Figure 2*, given that all PMTs in a row or column have the same ρ_y or ρ_x respectively, we can see that \mathbf{R} may be constructed in terms of δ as for example

$$\mathbf{R} = \frac{1}{N} \begin{pmatrix} \rho_{1x} & \rho_{2x} & 0 & 0 & 0 \\ 0 & 0 & \rho_{1y} & \rho_{3y} & \rho_{5y} \end{pmatrix} \delta = \frac{1}{N} \Gamma \delta \quad (15)$$

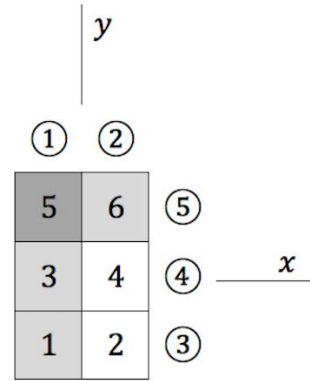


Fig 2. In a 2×3 PMT array, \mathbf{C} will have 6 elements, while δ will have 5. Indices corresponding to columns and rows (δ_i) are enclosed in circles. As an example, δ_1 and δ_5 have an intersection at C_{55} (over-highlighted).

So we have successfully expressed \mathbf{R} in terms of both the count values (\mathbf{C}) and the columns and row sums (δ) and Γ is the position of them. We add the nonlinear conditioning stage,

$$\mathbf{R} = \frac{1}{N} \Gamma g(\delta) \quad (16)$$

$g(\delta)$ is typically a nonlinear function thresholding both small and large values, markedly affecting the estimation performance. As before, we proceed to characterizing the performance by writing

$$E(\mathbf{R}) = \frac{1}{N} \Gamma . E(g(\delta)) \quad (17)$$

$$Cov(\mathbf{R}) = \frac{1}{N^2} \Gamma . Cov(g(\delta)) . \Gamma^T \quad (18)$$

Again we use equations (11)-(13) except that here we also need to find $PDF_{(\delta_i)}$ and $JOINT_{(\delta_i, \delta_j)}$. There will be a bit of combinatorics involved here as opposed to the straightforward case in \mathbf{C} , outlined next.

It can be seen from (14) that δ has two distinct parts, one corresponding to column sums and one to row sums. The two parts, each, are multinomial vectors according to the grouping property of a multinomial distribution (see *Appendix I-III* for complete proofs), with underlying probabilities in either part related through the same matrix Θ

$$\mathbf{J} = \Theta \mathbf{I} \quad (19)$$

Then $\delta = (\delta_1, \dots, \delta_\kappa)'$ also follows the multinomial distribution with probabilities \mathbf{J} and number N (\mathbf{I} is calculated by using of (1)).

However, as a whole, δ is not a multinomial vector; although with simple combinatorics to make adjustments, we can still use the multinomial vector properties.

δ_i in either part are part of multinomial distributions so their first marginal distributions would be straightforward:

$$\text{PDF}_{(\delta_i)}(k) = \text{Binom}_{(J_i)(1-J_i)}^{(k)(N-k)} \quad (20)$$

The case for joint probabilities is a bit more complicated. If δ_i and δ_j correspond to two rows or two columns – and not a mixture – then the joint distribution will be that of the usual multinomial distribution (see *Appendix I-II* for complete proofs), namely (21). But when δ_i and δ_j correspond to a row and a column (like δ_1 and δ_5 in *Figure 2*) resulting in an intersection hereby indexed t , then C_t needs to be accounted for separately, in the form of a summation over all possible values, namely (22).

$$\begin{aligned} & \text{JOINT}_{(\delta_i, \delta_j)}(k, l) \\ &= \begin{cases} \text{Multinom}_{(J_i)(J_j)(1-J_i-J_j)}^{(k)(l)(N-k-l)} & (21) \\ \sum_{m=0}^{\min(k,l)} \text{Multinom}_{(J_i-l_t)(J_j-l_t)(l_t)(1-J_i-J_j+l_t)}^{(k-m)(l-m)(m)(N-k-l+m)} & (22) \end{cases} \end{aligned}$$

The function actually used here, normalized to $(0,1)$, has been $g(x) = \text{ramp}(x * G(0.5,8) - 1/100)$, in which $G(\mu, \sigma^2)$ is the Gaussian function and the offset value $(1/100)$ determines the thresholding level. The function is again a slight variation of the identity function $h(x) = x$, slightly saturating towards the end, additional to an offset. The actual domain is $(0,N)$. Note that we are still working with the detector of *Figure 1*.

The numeric model

We can evaluate our analytical model thus far by comparing it against the simple numeric realization of the experiment, exactly as described in the “introduction” section.

With an assumed point source, each radiated photon is introduced by two spatial angles that determine its direction in space. To constitute isotropy, the two angles must follow a special distribution, rather than simple uniform distribution. All Photon incidence coordinates on the detector are calculated, then counted, and finally fed into the com{} positioning operator to produce the first point in the output image. This is rerun until a well-populated cloud of points is available, whose expected value and covariance matrix, μ and Q , are then calculated using simple statistics.

The detector specification

In this study, we consider a detector with NaI(Tl) rectangular crystal with the size of $40 \times 25 \text{ cm}^2$ area and 9.5 mm (3/8 inches) thickness attached to an 18-mm thick light-guide. The total area of the crystal covered by an array of PMT with different shape including square ($76 \times 76 \text{ mm}^2$), hexagonal (with 76 mm diameter) and circular (with 76 mm diameter).

Non-zero crystal thickness

Consider the scenario with a point gamma source, perfect collimator (that only passes rays normal to it), and a crystal with non-zero thickness. The depth at which scintillations will happen will no longer be deterministic, and will follow the exponential distribution

$$H(z) = \exp^{-\alpha z} \quad (23)$$

inside the crystal, with z being the depth measured from the crystal surface, and α the attenuation coefficient of NaI(Tl) crystal for 140 keV (1.76 cm^{-1}).

This scenario is a sample of a larger class of cases, in which a more thorough model of the system is required for proper analysis – one comprising more realistic versions of the source, collimator and crystal.

With c the crystal thickness, it is intuitive that the output image is expressible as

$$\Lambda = \int_0^c H(z)G(z)dz \quad (24)$$

Regarding evaluation with the numeric model, one modification needs to be made and that is the z coordinate of the source shall no longer be fixed, but has to be a random variable with the distribution $H(z)$ bound to the crystal thickness.

Evaluation

We may use as an evaluation basis the fact that the three methods – the linear method along with the two nonlinear ones (eqs. (4), (9), (16)) – should yield the same result if the non-linear functions are set to $f(x) = g(x) = x$. Note that this will not be trivial as the three methods involve radically different algorithms and calculations.

One issue that needs to be pointed out regarding the light media (crystal and light-tube) is that all lateral faces are assumed to be perfect absorbers and the top face – from which gamma rays enter – to be a perfect mirror. In all simulations thus far, whether there explicitly exist a crystal and light-tube or not, the reflection from where the mirror would be has been taken into account. This has been done by adding an imaginary source to the other side of the mirror, with

each of the two sources having half the number of photons, scintillating downwards only.

RESULTS

Due to symmetry, for any analysis of the camera we consider only a quarter of the detector, as highlighted in Figure 1. The constructed figures are composed of two rows. The top row contains scatter maps showing the positioning output for uniform grid inputs that were originally distributed over $x \in (0, 2D)$ and $y \in (0, 3D)$. The bottom row contains resolution maps showing the blurring intensity corresponding to each position evaluated over the same input grid. Blurring intensity is reported as FWHM in mm that obtained using (7), (12).

In the Figure 3, we considered the detector, as described in the section 0, with square PMTs and simple center of mass as the positioning method. The effect of dead-zones of every PMT (10 mm into the PMT from each side) was showed that in the Figure 3B compared to Figure 3A that we considered perfect PMT without any dead-zones. We showed that the effect of different size of PMTs on the scatter map and resolution in the Figure 4. Same as Figure 3, the simple center of mass method is applied to find the position of interaction.

The effect of different positioning method was showed in Figure 5. All of these simulations we considered the square PMTs with 76×76 mm² dimensions. The basic Anger method, nonlinear Anger method with thresholding and the CSE method are applied to find the position of interaction.

For comparison of analytical and numerical model, at a sample source position, say $(x_0, y_0, z_0) = (50.7, 50.7, 23.5)$, the analytical model makes the following prediction:

$$E\{\mathbf{R}\} = \begin{pmatrix} 42.3 \\ 45.7 \end{pmatrix}, \text{Cov}\{\mathbf{R}\} = \begin{pmatrix} 0.48 & 0.01 \\ 0.01 & 0.65 \end{pmatrix}. \quad (25)$$

On the numerical side, it is observed that the statistical estimations of the expected value ($\boldsymbol{\mu}$) and covariance matrix (\mathbf{Q}) approach the values in (25) as the number of points of the cloud is increased. Specifically, with around 2200 points, the averages in four consecutive runs equal those in (25) down to four decimal places. The same happens at any arbitrary source position, meaning that the above evaluation test is passed.

DISCUSSION

Starting with the first scatter map, Figure 3A, we can make some general observations. The grid is jammed near the edges. Grid rows and columns, albeit mainly incurred, exhibit variant spacing and consequently slight pincushion effect. As always the whole image is

somewhat minimalized. In Figure 3B, the non-uniform PMT response introduces a distortion into the scatter map. Resolution is markedly deteriorated, less at PMT centers and more at borders, although the overall pattern remains unchanged. This is intuitive given the specific shape of the response used here. It should be noted we considered about 45% of the area of each PMT as the dead-zones; this amount is about 15% in reality but the exaggerated amount can help us to better present its effect on the resolution. In Figure 3C, the lower gain introduces a swelling in the scatter map, again obvious because, when the PMT is involved with less weight in the center of mass calculation, outputs are more readily drawn to neighboring centers. As for the resolution map, except for a local deterioration over the troubled PMT, the resolution has remained largely unaffected. In Figure 3D, addition of crystal thickness and attenuation appears to have negligible effect on the scatter map. It is compatible to reality because the effect of DOI in gamma rays with energy less than 400 keV, are commonly used in the gamma camera, is negligible [14-17]. In the resolution map, shadow-like artefacts appear, and the worst-resolution sites are slightly displaced from PMT borders. Note that scintillations happen at the “expected depth” in Figure 3A, and in their real “extended dimensions” in Figure 3D. Note that the expected depth means free path of 140 keV in the NaI(Tl) crystal that is 3.98 mm.

In Figure 4, we present how the PMT shape can affect both linearity and resolution. The basic positioning method was applied in all of simulations in Figure 4. The worst resolution among all of shape of PMTs belongs to square PMTs, as show in Figure 4A to C. The main hypothesis in basic positioning method (or Anger) is that the distance from the center of one PMT to the center of neighboring PMTs should be the same in all directions. This assumption is not met in the square PMTs because of the four PMTs touching the sides of the center PMT are significantly closer than the four touching the corners only.

In Figure 4B, PMT centers are no longer aligned and attraction towards centers translates to curved distortions. There is fringing near the edges, following centers of the outermost PMTs. The hexagonal configuration has resulted in considerable enhancement of resolution. In Figure 4C, there is slightly worse distortion (more attraction towards centers, and naturally fringing) and slightly enhanced resolution.

As we expected, the square PMTs introduces the best quality of scatter map near the edges. In Figure 4D, source further away results in much better uniformity and less edge fringing, in exchange for increased minimalisation and a completely undermined resolution.

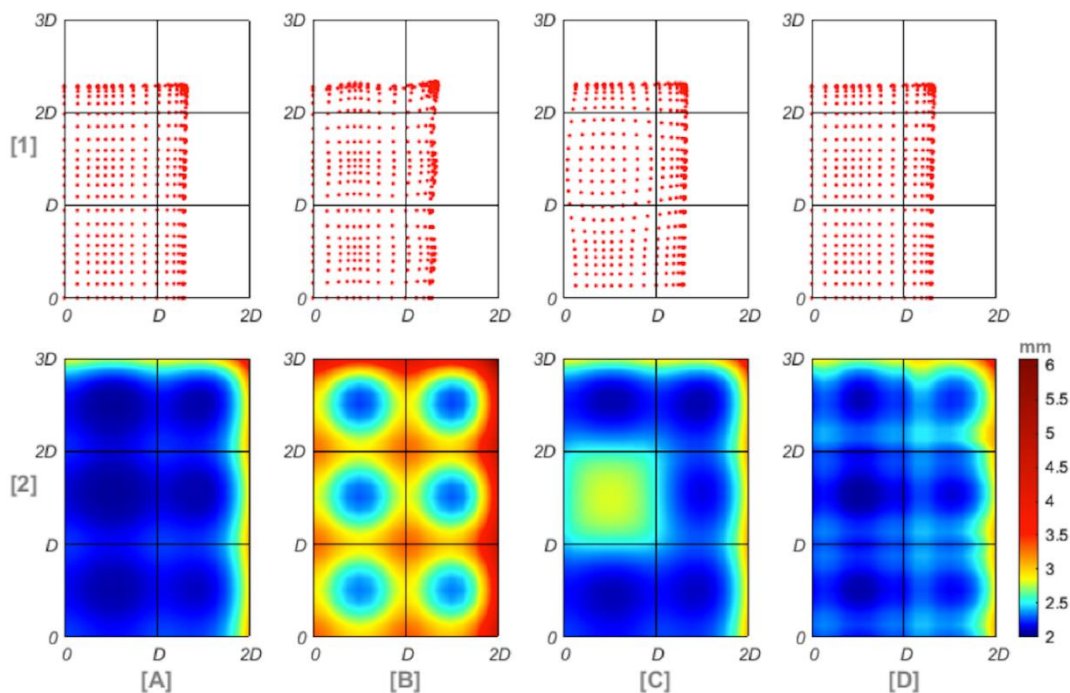


Fig 3. One quarter of the detector in Fig 1. TOP Scatter-maps showing the positioning output for uniform grid inputs. BOTTOM Resolution maps showing the blurring intensity corresponding to each position, in mm FWHM. [A] The basic case, [B] PMTs have dead-zones near their boundaries, [C] one PMT has half unit gain, [D] the crystal has non-zero thickness.

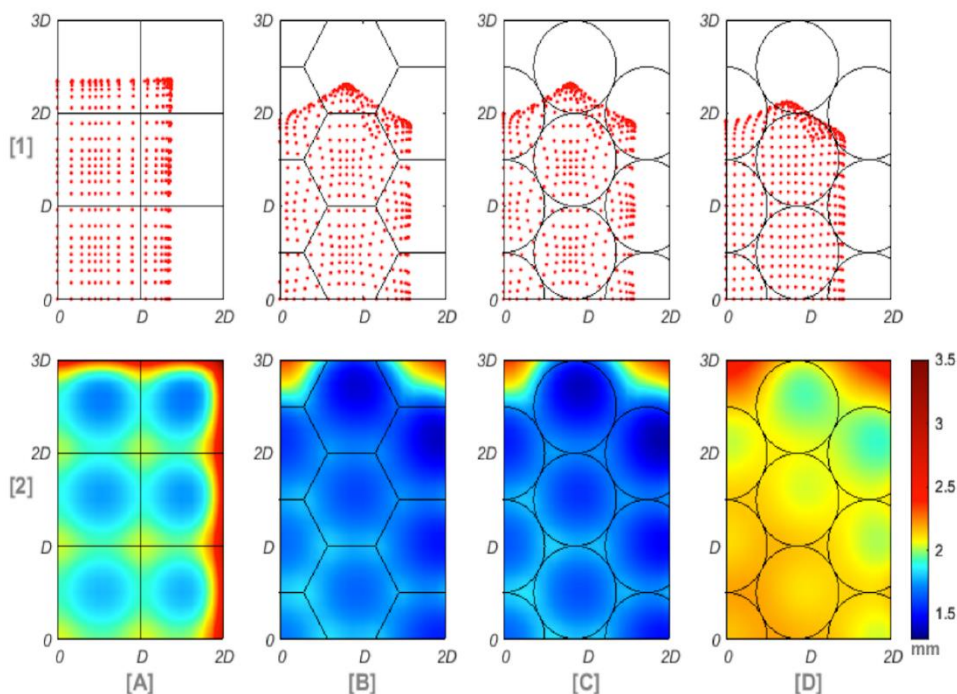


Fig 4. The scatter maps and FWHM using simple center of mass as positioning method and using different shape of PMTs including [A] Square, [B] Hexagonal, [C] Circular and [D] the source is moved away to 4/3 the default.

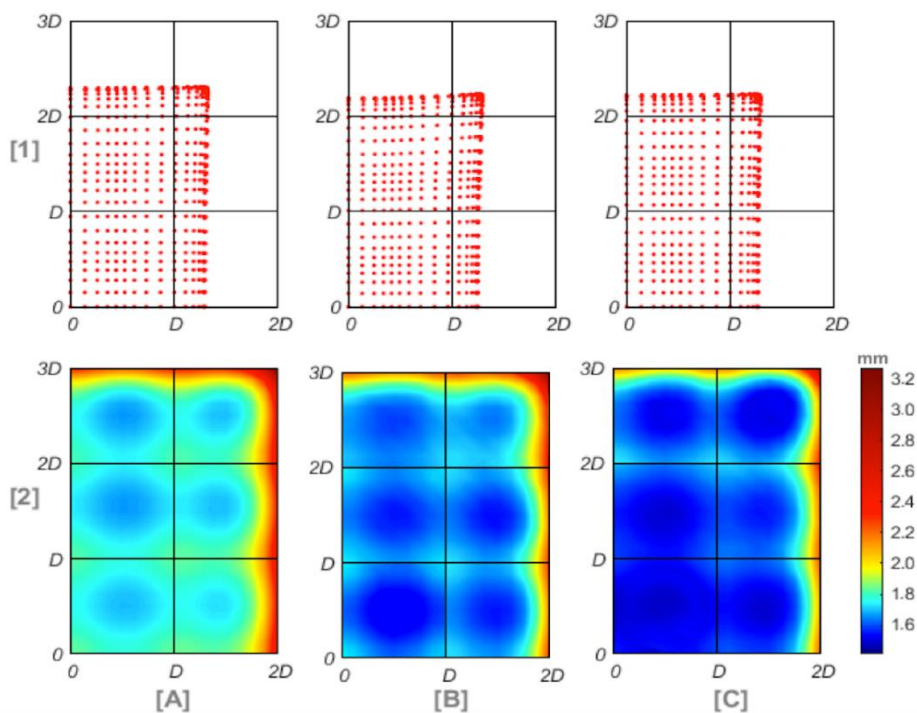


Fig 5. Scatter maps and FWHM maps were calculated using different positioning techniques including [A] basic Anger, [B] nonlinear Anger, and [C] CSE. Number of photons used is $N=85$.

It should be noted that we cannot easily judge which method is performing better solely based on the resolution maps, until a linearity correction stage is first applied; i.e. we may only judge the resolution maps when the linearity maps are similar, because otherwise you can always get perfect resolution at the expense of complete destruction of linearity and positioning.

The experiment in Figure 5A is identical to Figure 3A in all respects except for the smaller $N=85$ here instead of 5600. Blurring intensities must therefore be related through the factor $\sqrt{(5600/85)}$, and comparing the two figures, they exactly are. The scatter maps on the other hand show expected values of output locations, disregarding statistical noise caused by finite N , and hence are the same in the two figures. In Figure 5B-C, raw resolutions improve with non-linear methods, while distortions are introduced at the same time. With parts A and C that have visually more or less similar linearity maps it is apparent how employment of non-linear methods can enhance resolution considerably.

It is noteworthy that the analytical and numerical methods are fundamentally different approaches and the production of identical results proves that the analytical model correctly captures the dynamics of the problem.

CONCLUSION

Since the rectangular shape of the scintillation crystal is the most compatible geometry considering the contour of human body, we showed that the square PMT is the best design demonstrating better image quality specially near the edge of the detector. Another advantage of square PMTs is the minimization of required PMT number to cover the crystal area.

Also, we showed that the Anger method cannot work properly in case of using square PMT. We applied two nonlinear positioning methods to improve the linearity and resolution using square PMT. The CSE method resulted in considerable enhancement of resolution at the same time significant reduction of distortion.

In this study, we showed that the gamma camera with rectangular crystal equipped with an array of square PMTs applying the CSE method can be adequate design specially in the applications of the SPECT imaging. It should be noted that the gamma camera with the presented design has been developed and assessed its image quality for practice according to NEMA standard [18].

Acknowledgments

This work was supported under grant number 28212, Tehran University of Medical Sciences, Tehran, Iran, and Amirkabir (Tehran Polytechnic) University of Technology, Tehran, Iran.

Appendix I: The multinomial distribution

If a given trial (e.g. landing of a single photon on the detector) can result in the k outcomes O_1, O_2, \dots, O_k with probabilities I_1, I_2, \dots, I_k , then the probability distribution of the random variables C_1, C_2, \dots, C_k representing the number of occurrences for O_1, O_2, \dots, O_k in N independent trials is

$$\text{Multinom}_{(I_1)(I_2)\dots(I_k)}^{(C_1)(C_2)\dots(C_k)} = \binom{N}{C_1, C_2, \dots, C_k} I_1^{C_1} I_2^{C_2} \dots I_k^{C_k}$$

where

$$\sum_{i=1}^k C_i = N, \quad \sum_{i=1}^k I_i = 1.$$

I. Moments: For the random vector \mathbf{C} following the multinomial distribution with underlying probabilities arranged in vector \mathbf{I} and number of experiments N , we know

$$E(C_i) = NI_i, \quad \text{Var}(C_i) = NI_i(1 - I_i), \\ \text{Cov}(C_i, C_j) = -NI_i I_j$$

Using these values we can construct the moments $E(\mathbf{C})$ and $\text{Cov}(\mathbf{C})$. Note that the covariance matrix of the vector $\mathbf{C}_{(k \times 1)}$ is the symmetrical matrix $\mathbf{M}_{(k \times k)}$ whose diagonal and non-diagonal elements are

$$M_{ii} = \text{Var}(C_i) \text{ and } M_{ij} = \text{Cov}(C_i, C_j).$$

II. Marginal distributions:

$$\text{PDF}_{(C_i)}(k) = \text{Binom}_{(I_i)(1-I_i)}^{(k)(N-k)}$$

$$\text{JOINT}_{(C_i, C_j)}(k, l) = \text{Multinom}_{(I_i)(I_j)(1-I_i-I_j)}^{(k)(l)(N-k-l)}$$

III. Grouping property: The multinomial distribution is preserved when the counting variables are combined. Specifically, suppose that (A_1, \dots, A_k) is a partition of the index set $(1, \dots, k)$ into nonempty subsets. For $j \in (1, \dots, k)$ let

$$\delta_j = \sum_{i \in A_j} C_i, \quad J_j = \sum_{i \in A_j} I_i$$

then $\boldsymbol{\delta} = (\delta_1, \dots, \delta_k)'$ also follows the multinomial distribution with probabilities \mathbf{J} and number N

REFERENCES

1. Anger HO. Scintillation camera. Rev Sci Instrum. 1958;29(1):27-33.

2. Anger HO. Scintillation camera with multichannel collimators. J Nucl Med. 1964 Jul;5:515-31.

3. Bushberg JT, Seibert JA, Leidholdt EM, Boone JM. Essential physics of medical imaging. 2nd ed. Philadelphia: Lippincott Williams & Wilkins; 2002.

4. Peterson TE, Furenlid LR. SPECT detectors: the Anger camera and beyond. Phys Med Biol. 2011 Sep 7;56(17):R145-82.

5. Svedberg JB. On the intrinsic resolution of a gamma camera system. Phys Med Biol. 1972 Jul;17(4):514-24.

6. Svedberg JB. Computer simulation of the Anger gamma camera. Comput Programs Biomed. 1975 Mar;4(3):189-201.

7. Svedberg JB. Image quality of a gamma camera system. Phys Med Biol. 1968 Oct;13(4):597-610.

8. Baker RG, Scrimger JW. An investigation of the parameters in scintillation camera design. Phys Med Biol. 1967 Jan;12(1):51-63.

9. Hunter WCJ. Modeling stochastic processes in gamma-ray imaging detectors and evaluation of a multi-anode PMT scintillation camera for use with maximum-likelihood estimation methods. PhD thesis. Department of Physics, The University of Arizona; 2007.

10. Sain JD. Optical modeling, design optimization, and performance analysis of a gamma camera for detection of breast cancer. PhD thesis. The University of Arizona; 2001.

11. Barrett HH, Hunter WC, Miller BW, Moore SK, Chen Y, Furenlid LR. Maximum-likelihood methods for processing signals from gamma-ray detectors. IEEE Trans Nucl Sci. 2009 Jun 1;56(3):725.

12. Fessler JA. Statistical image reconstruction methods. In: Fitzpatrick JM, Sonka M. Handbook of medical imaging, volume 2. Medical image processing and analysis. Spie Press Book;2000. P. 1-71.

13. Jansen FP, Binnie DM. Signal processing in scintillation cameras for nuclear medicine. Patent 5,504,334, 1996.

14. Anger HO. Sensitivity, resolution, and linearity of the scintillation camera. IEEE Trans Nucl Sci. 1966;13(3):380-392.

15. Tanaka E, Hiramoto T, Nohara N. Scintillation cameras based on new position arithmetics. J Nucl Med. 1970 Sep;11(9):542-7.

16. Hwang AB, Iwata K, Hasegawa BH. Simulation of depth of interaction effects for pinhole SPECT. IEEE Nucl Sci Symp Conf Rec. 2001;3:1293-1297.

17. Korevaar MAN. High-resolution EM-CCD scintillation gamma cameras. PhD thesis. Delf University of Technology; 2013.

18. Zeraatkara N, Sajedia S, Teimourian Farda B, Kaviania S, Akbarzadeh A, Farahani MH, Sarkar S, Ay MR. Development and calibration of a new gamma camera detector using large square photomultiplier tubes. J Instrum. 2017;12(9):P09008.